Electronic Supplementary Information

for

Advances in photo-assisted seawater splitting promoted by green iron oxide-carbon nitride photoelectrocatalysts

Mattia Benedet,[ab] Gian Andrea Rizzi,[*ab] Oleg I. Lebedev,[c] Vladimir Roddatis,[d] Cinzia Sada,[e] Jan-Lucas Wree,[f] Anjana Devi,[f] Chiara Maccato,[*ab] Alberto Gasparotto[ab] and Davide Barreca[b]

[a] *Department of Chemical Sciences, Padova University and INSTM, 35131 Padova, Italy*

[b] *CNR-ICMATE and INSTM, Department of Chemical Sciences, Padova University, 35131 Padova, Italy*

[c] *Laboratoire CRISMAT, UMR 6508 Normandie Université, CNRS, ENSICAEN, UNICAEN, 14050 Caen Cedex 4, France*

[d] *GFZ German Research Centre for Geosciences, 14473, Potsdam, Germany*

[e] *Department of Physics and Astronomy, Padova University and INSTM, 35131 Padova, Italy*

[f] *Inorganic Materials Chemistry, Ruhr University Bochum, 44801 Bochum, Germany*

* Corresponding authors. E-mail: gianandrea.rizzi@unipd.it; chiara.maccato@unipd.it.

§ S-1. Experimental

§ S-1.1 Synthesis

§ S-1.1.1 α-Fe$_2$O$_3$ preparation

Plasma enhanced-chemical vapor deposition (PE-CVD) growth processes were performed using a two-electrode custom-built apparatus equipped with a radio frequency (RF) generator (v = 13.56 MHz), adopting Fe(tfa)$_2$TMEDA (tfa = 1,1,1-trifluoro-2,4-pentanedionate; TMEDA = *N,N,N',N'*-tetramethylethylenediamine) as iron precursor.[1] Fluorine-doped tin oxide (FTO) glass substrates (Aldrich®; ≈ 7 Ω/sq; FTO thickness ≈ 600 nm), subjected to an established pre-cleaning procedure,[2] were mounted on the grounded electrode of the PE-CVD reactor, whereas RF-power was applied to the second electrode. Electronic grade Ar and O$_2$ were used as plasma sources. The precursor powders were placed in an external glass reservoir heated at 85°C by an oil bath, and the vapors were delivered to the deposition zone by an Ar flow [rate = 60 standard cubic centimetres per minute (sccm)] maintaining the feeding lines at 150°C. Two additional gas-lines were used to introduce Ar (rate = 15 sccm) and O$_2$ (rate = 5 sccm) directly into the reactor. For all depositions, the inter-electrode distance, total pressure, RF-power and process duration were fixed at 6 cm, 1.0 mbar, 20 W and 90 min, respectively. The growth temperature was varied between 100 and 400°C.

§ S-1.1.2 Carbon nitride preparation

In this work, two different types of graphitic carbon nitride (gCN) powders were prepared using as precursor either melamine [gCN(M)] or a mixture of melamine and cyanuric acid [gCN(CM)]. The former was obtained by melamine (M – Sigma Aldrich) heat treatment in Ar atmosphere at 400°C for 2 h, to activate melamine condensation to tri-s-triazine, and subsequently at 550°C for 4 h, to trigger polymerization processes yielding carbon nitride.[3] Alternatively, following the synthetic route proposed by Jun *et al.*[4], melamine (M – 1.0 g) and cyanuric acid (CA – Sigma Aldrich; 1.0 g) were dispersed under sonication in 40 mL and 20 mL of dimethylsulfoxide (DMSO), respectively. After heating at 60°C, the CA-containing mixture was dropped into the M one under continuous stirring, yielding a white suspension of the supramolecular M+CA adduct (CM adduct). After 10 min, the suspension was filtered, and the obtained powder was washed twice with 10 mL ethanol. The recovered solid was heated in Ar at 50°C for 3 h, and, subsequently, at 500°C for 2.5 h.

During each electrophoretic deposition (EPD) experiment, the gCN suspension was always maintained under stirring. After a series of preliminary experiments aimed at optimizing the operational conditions and at ensuring the reproducibility of material characteristics, a duration of 20 s was utilized. A potential difference of 10 V was applied using an Agilent E3649A bench power supply. At the end of the process, an ex-situ two-step thermal treatment in air was performed: 1) annealing at 80°C for 1 h (heating rate = 3°C/min); 2) annealing at 520°C for 3 h (heating rate = 20°C/min), followed by a slow cooling to room temperature.

§ S-1.1.3 Functionalization with CoPi

A Co(II) phosphate solution (0.005 M) was prepared by dissolving 16.22 mg of $CoCl_2 \bullet 6H_2O$ in 250 mL of a phosphate buffer solution at pH = 7.0. The CoPi deposition procedure on the target photoanodes, optimized basing on the strategy suggested by Nocera et al.,[5] was performed as follows:

• 1 CV (cyclic voltammetry) in phosphate buffer (pH = 7.0);

• 1 CV in Co(II) 0.005 M solution in phosphate buffer;

• 1 LSV (linear scan voltammetry) in Co(II) 0.005 M solution in phosphate buffer.

For each scan, a potential range from 0.2 to 1.2 V was adopted.

§ S-1.2 Chemico-physical characterization

X-ray diffraction (XRD) characterization was carried out in glancing incidence mode (θ_i = 1.0°) on a Bruker AXS D8 Advance Plus diffractometer equipped with a Göbel mirror and a CuKα X-ray source (λ= 1.54051 Å) powered at 40 kV and 40 mA. The analyses were performed at the PanLab facility (Department of Chemical Sciences, Padova University) founded by the MIUR Dipartimento di Eccellenza grant "NExuS".

Optical absorption spectra were recorded operating in transmittance mode at normal incidence on a Cary 50 (Varian) dual-beam spectrophotometer (spectral bandwidth = 1 nm), using a bare FTO-coated glass substrate as a reference. In all cases, the substrate contribution was subtracted. The band gap (E_G) of Fe_2O_3-containing samples was evaluated using the Tauc relation:[6-9]

$$(\alpha h\upsilon)^n = K(h\upsilon - E_G) \tag{S1}$$

where α, $h\upsilon$ and K are the absorption coefficient, the photon energy and a constant, respectively,

and $n = 2$ for direct allowed transitions, reported to be the strongest ones for *hematite*,[10] the main system component. E_G values were obtained by extrapolating the straight portion of experimental curves to intersect the energy axis at $\alpha = 0$.

For transmission electron microscopy (TEM) analyses, thin cross-sectional samples were prepared using a Thermo Fischer Scientific Helios G4 UC dual beam instrument, located at the PISA facility (GFZ, Potsdam) by the focused ion beam (FIB) technique (Fig. 4 in the main paper). Prior to FIB cutting, a part of the specimen was coated with a liquid silicon glass (Baufan Kali-Wasserglas) to prevent any possible contamination. In the preparation of samples, a Pt layer was deposited to minimize undesired damages/alterations, due to gCN nanostructures fragility under ion beam irradiation. Additional specimens were prepared by scratching, ultrasonication in ethanol and subsequent dispersion on TEM Cu holey carbon grids (see Fig. S12).

As a matter of fact, Fe 2p X-ray photoelectron spectroscopy (XPS) signal deconvolution poses a number of complications. In fact, a reliable fitting must take into account shake-up and plasmon loss structures, as well as multiplet splitting phenomena, all of which can complicate chemical state identification.[11] As a consequence, in the present study curve fitting of Fe 2p spectra was intentionally avoided. Nevertheless, it is worthwhile highlighting that the XPS results presented and discussed in this work unambiguously indicate the occurrence of Fe_2O_3 free from other iron oxides in appreciable amounts, in line with the results obtained by the other characterization techniques.

XPS and ultraviolet photoelectron spectroscopy (UPS) valence band spectra were taken after a mild Ar^+ erosion (2000 eV, 30 s) using a ThermoFisher Scientific ESCALB^{TM} QXi spectrometer funded by "Sviluppo delle infrastrutture e programma biennale degli interventi del Consiglio Nazionale delle Ricerche (2019). A monochromatic AlKα X-ray source and a He(I) ($h\nu = 21.22$ eV) ultraviolet photon source generated by a helium plasma lamp were employed to collect XPS and UPS valence band spectra, respectively.

Photoluminescence (PL) spectra were recorded using a FLS 1000 fluorimeter (Edinburgh Instruments), adopting the following settings: excitation wavelength/bandwidth = 280/13 nm; emission bandwidth = 7 nm.

§ S-1.3 Photolectrochemical tests and related analyses

The measured potential was converted into the reversible hydrogen electrode (RHE) scale using

the following relation:[6]

$$E_{RHE} (V) = E_{WE} (V) + E_{Ag/AgCl} (V) + 0.0592 \times pH \qquad (S2)$$

where E_{WE} indicates the bias applied to the working electrode.

The obtained E_{RHE} values were subjected to iR correction according to equation (S3):[12]

$$E (V) = E_{RHE} (V) - iR \qquad (S3)$$

where i is the measured current (in A), and R the uncompensated cell resistance. The latter was estimated from electrochemical impedance spectroscopy (EIS) as the lowest impedance observed in the high-frequency region of Nyquist plots.[13] For all photoelectrocatalysts, the uncompensated resistance ranged between $\approx$90 and 100 Ω. These relatively high resistance values are likely due to the contact between the FTO-supported electrode and the copper foil pressed on its surface, as sketched in Fig. S1. For each electrode, the registered currents were normalized to the geometric sample area ($\approx$0.28 cm^2).
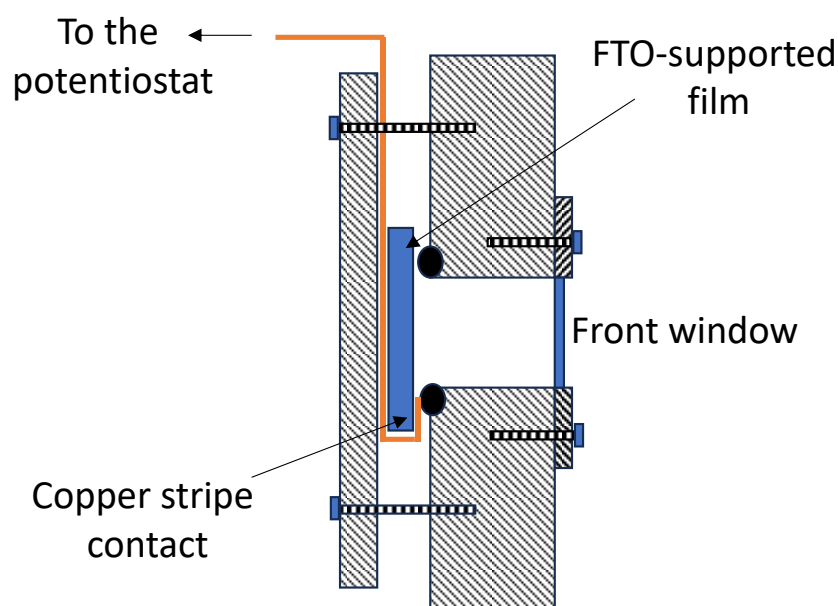
Fig. S1. Side-view of Zahner photoelectrochemical cell, showing the electrical contact between the copper stripe and the working electrode.

The onset potential was calculated as the one necessary to reach a photocurrent density of 0.02 mA/cm^2.[14]

Intensity modulated photocurrent spectroscopy (IMPS) analyses were carried out applying a

LED frequency between 10000 and 0.05 Hz with a 15% of light intensity modulation. The white light intensity was set at 50 mW/cm^2.

EIS spectra were acquired from 100 mHz to 10 kHz with a potential modulation of 5 mV.

Mott-Schottky plots were obtained at 1 kHz by recording EIS spectra between 0.4 and 1.6 V *vs*. RHE, with 0.1 V steps. The capacitance value (C_{sc}) was obtained from Z = R + 1/(iωC_{sc}), where Z and R are the specimen impedance and resistance, and ω is the frequency. The flatband potential (V_{FB}) was measured by fitting the linear part of $1/C_{sc}^2$ and finding the intercept with the voltage axis, using the equation:[2, 15, 16]

$$\frac{1}{C_{SC}^2} = \frac{2}{\varepsilon_0 \varepsilon_r e N_D}\left(V - V_{FB} - \frac{k_B T}{e}\right) \tag{S4}$$

where C_{SC} is the capacitance of the semiconductor ($1/C_H^2$, capacitance of the double layer, is considered negligible), ε_0 the permittivity of free space, ε_r is relative permittivity of the target material, e is the electron charge (C), and k_B is the Boltzmann constant. The majority carrier concentration (N_D) was obtained from the slope of the linear part of $1/C_{SC}^2$. The value for the Fermi level energy (E_F) was assumed to be coincident with V_{FB} and was used to construct the diagram of Fig. 6.[16]

Iodometric titration was used for the identification of possible hypochlorite species generated during the process, following a previously described procedure.[6] In this case, ClO$^-$, if present, oxidizes I$^-$ species in alkaline solution according to the reaction:

$$H_2O + ClO^-_{(aq)} + 2I^-_{(aq)} \rightarrow I_2 + Cl^-_{(aq)} + 2OH^-_{(aq)} \tag{S5}$$
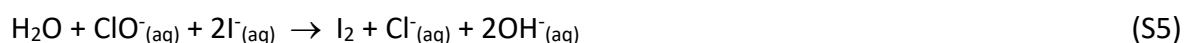
The obtained I$_2$ subsequently forms polyiodide ions, like I$_3^-$, that in the presence of starch yield an intensely blue colored complex.[17] The appearance of the latter can be considered as a finger-print of hypochlorite presence.

§ S-2. Characterization

§ S-2.1 Optimization of iron(III) oxide growth conditions

In this work, preliminary attention was devoted to the optimization of iron(III) oxide growth by PE-CVD, with particular regard to the evolution of material structural, morphological and optical properties as a function of the adopted preparative conditions. The system structure was investigated by XRD. As can be observed in Fig. S2, whereas at 100°C no diffraction peaks were evident, for temperatures $\geq$ 200°C the recorded patterns were characterized by reflections pertaining to rhombohedral α-Fe_2O_3 (*hematite*) as the sole iron(III) oxide polymorph.[18] A comparison with the reference pattern suggested a preferential (110) growth for $T \geq$ 300°C, that may account for an improved electron transport, resulting in enhanced photoelectrochemical performances.[10]
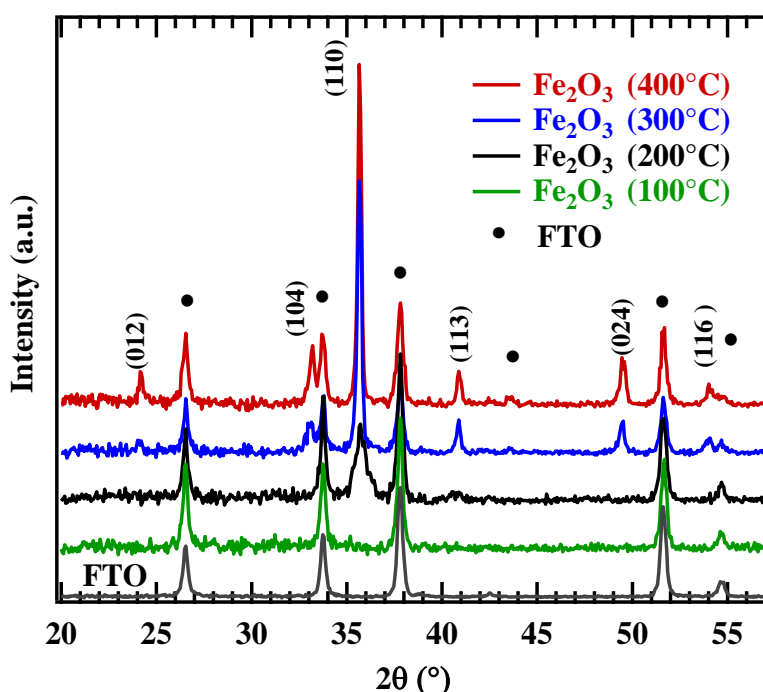
Fig. S2. XRD patterns of Fe_2O_3 deposits on FTO obtained at different growth temperatures. The pattern pertaining to the FTO-coated glass substrate is also reported for comparison. All the indexed peaks correspond to α-Fe_2O_3 (*hematite*) reflections.[18]

Optical absorption spectra (Fig. S3), consistent with those previously reported for pure iron(III) oxide nanomaterials,[10] showed a progressive absorbance increase with deposition temperature throughout the whole wavelength range. The calculated optical band gaps (E_G = 2.08 $\pm$ 0.06 eV) were in good agreement with those for Fe_2O_3.[2]
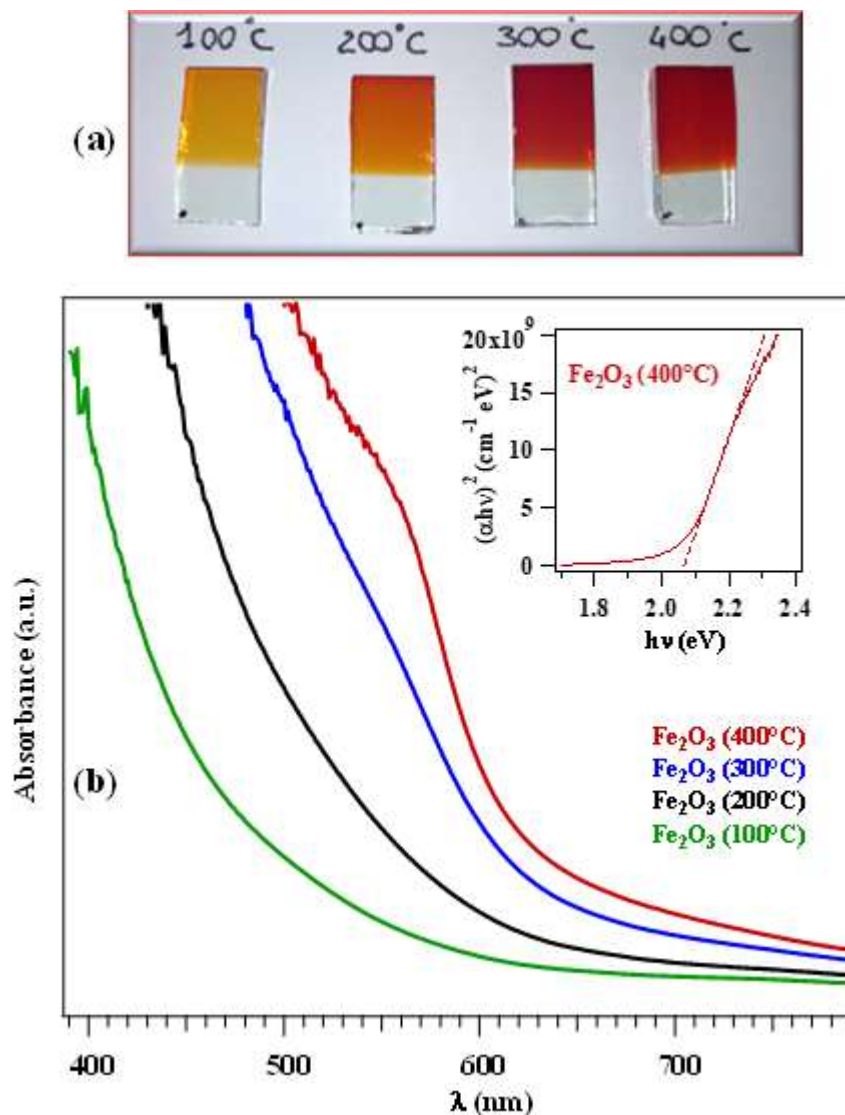
Fig. S3. (a) Digital photograph of Fe_2O_3 samples grown at different temperatures. (b) Optical absorption spectra of the same specimens. Inset: Tauc plot of the sample deposited at 400°C.

The system morphological features were investigated by field emission-scanning electron microscopy (FE-SEM, Fig. S4]. The specimen obtained at 100°C featured a compact globular organization, whereas at 200°C the deposit presented interconnected wheat-ear shaped structures perpendicular to the FTO substrate surface. In a different way, specimens prepared at 300°C and 400°C presented lamellar aggregates, whose assembly resulted in high active area materials. The latter can favor gCN dispersion even in the inner sample regions, promoting a close Fe_2O_3/gCN contact. In addition, their hierarchical porous structure offers a short diffusion channel for ion and mass transportation, highly beneficial for seawater penetration.[13]

Basing on the above data, the sample grown at 400°C was selected as the most promising one

for the subsequent functionalization with gCN and CoPi thanks to its higher crystallinity, improved optical absorption, and favorable morphological features.
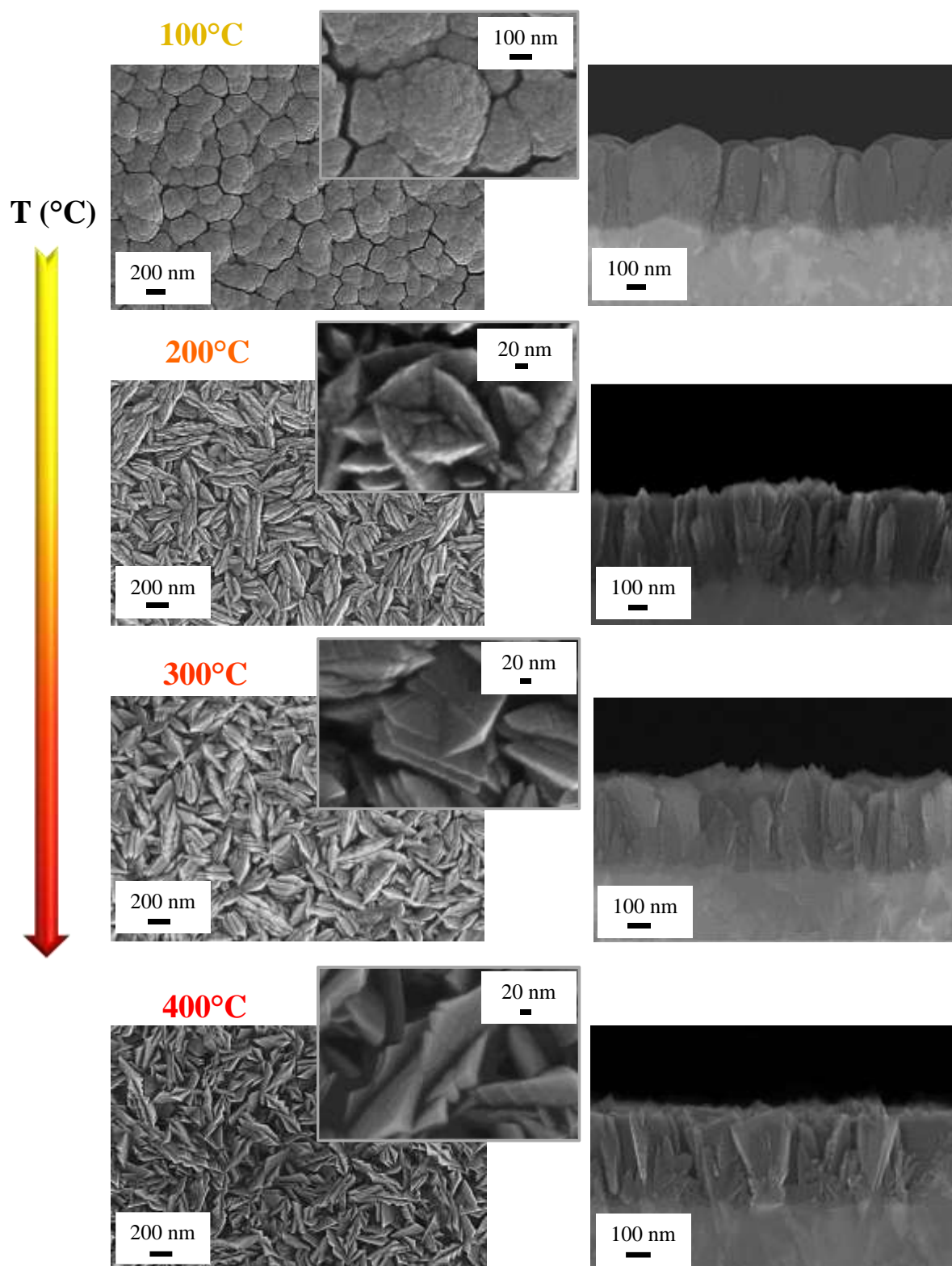
Fig. S4. Representative plane-view (left) and cross-sectional (right) FE-SEM images of Fe_2O_3 deposits grown on FTO at different temperatures.

§ S-2.2 Chemico-physical characterization of electrode materials

	weight%			
Sample	**C Kα**	**N Kα**	**O Kα**	**Fe Kα**
Fe₂O₃-M	3.0	4.0	50.0	43.0
Fe₂O₃-CM	4.0	3.8	49.5	42.7
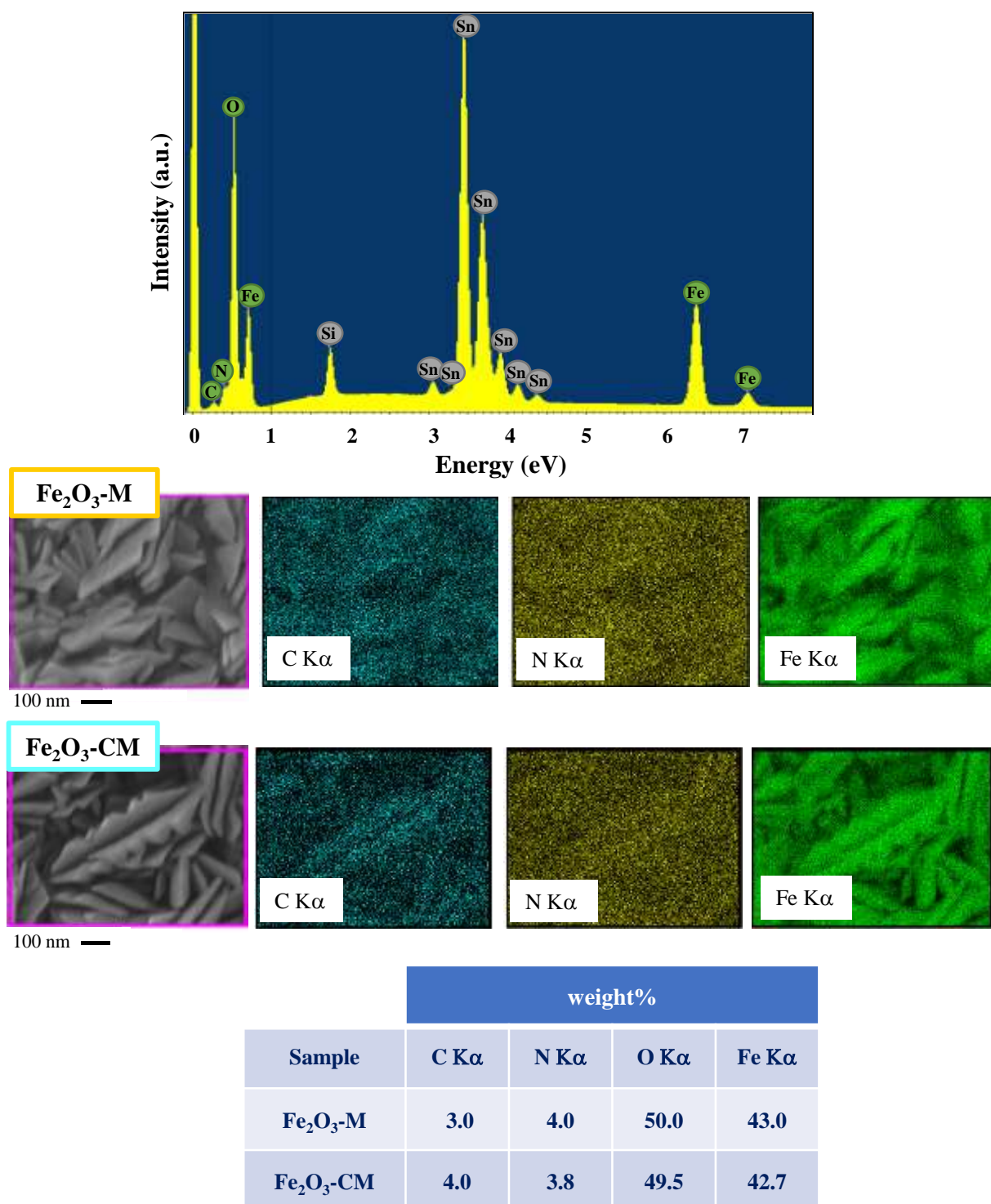
Fig. S5. Top: representative energy-dispersive X-ray spectroscopy (EDXS) spectrum for a Fe₂O₃-CM specimen. Bottom: plane view FE-SEM images, corresponding EDXS maps on the selected areas, and related quantitative analyses for Fe₂O₃-M and Fe₂O₃-CM. C and O contents are also affected by adventitious contamination (see XPS results) and the underlying FTO substrate, respectively.
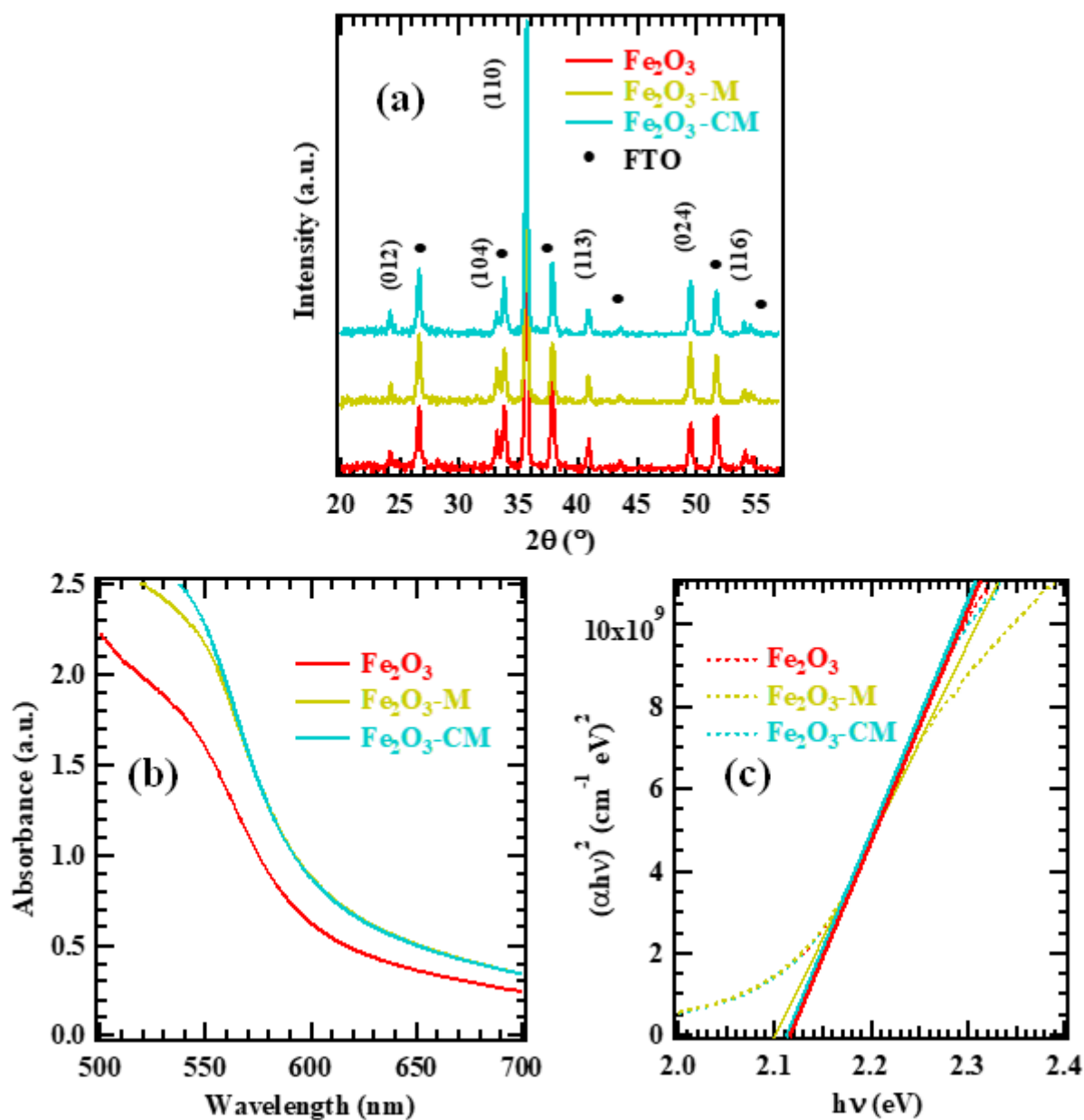
Fig. S6. (a) XRD patterns, (b) optical absorption spectra, and (c) Tauc plots of Fe_2O_3, Fe_2O_3-M and Fe_2O_3-CM specimens.
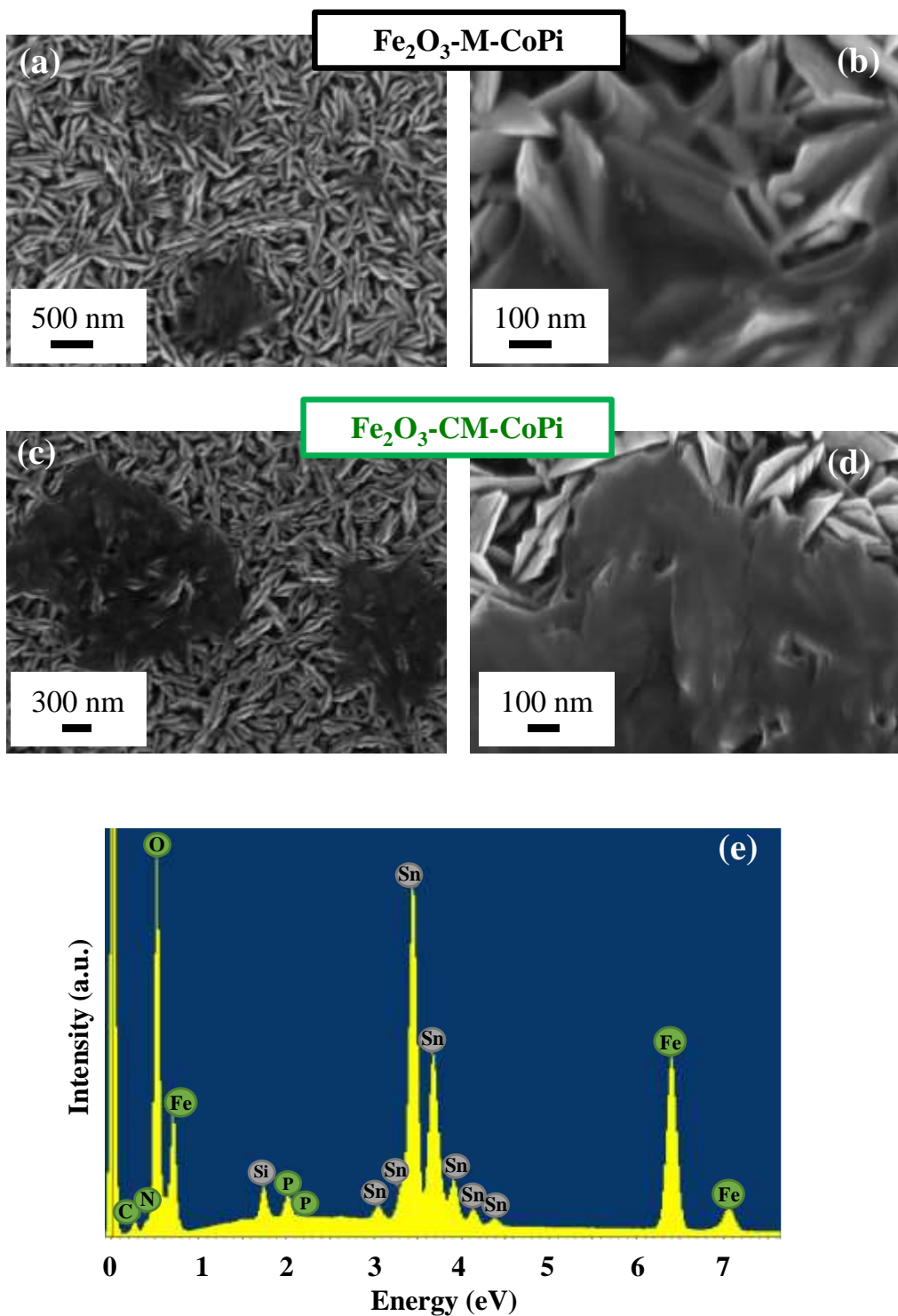
Fig. S7. Representative FE-SEM images for specimens Fe$_2$O$_3$-M-CoPi (a,b) and Fe$_2$O$_3$-CM-CoPi (c,d). (e) EDXS spectrum for sample Fe$_2$O$_3$-CM-CoPi. Phosphorus presence confirms the successful system functionalization with CoPi.

FE-SEM images in Fig. S7a-d demonstrate that CoPi deposition leads to aggregates homogeneously distributed over the underlying deposits and featuring various shapes and dimensions. CoPi presence is also demonstrated by EDXS analyses (Fig. S7e).
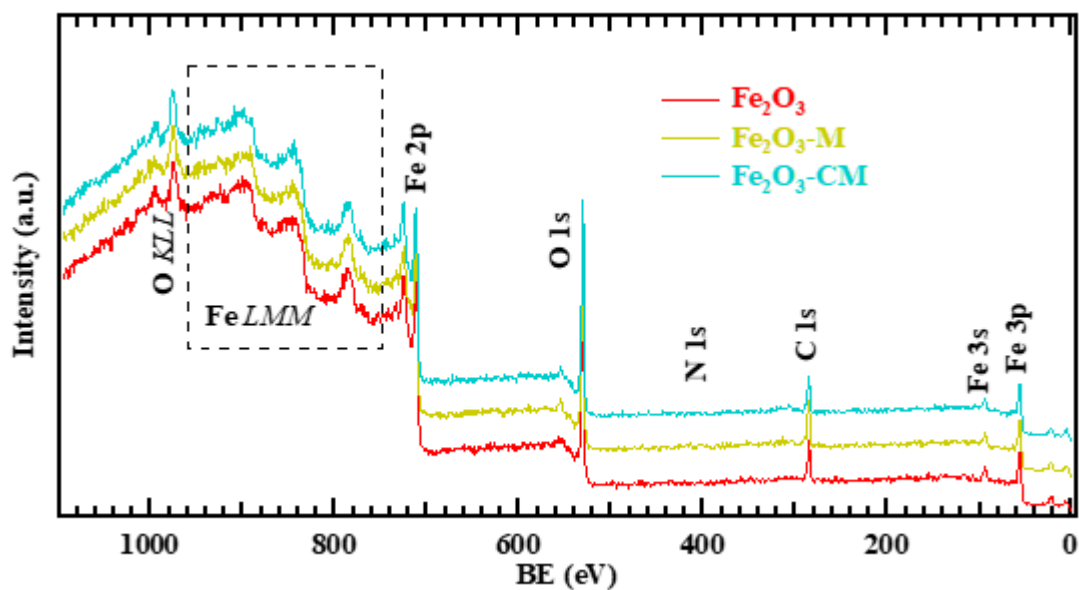
Fig. S8. XPS wide scan spectra for bare Fe_2O_3 and gCN-functionalized specimens.

XPS wide scan spectra (Fig. S8) clearly show iron and oxygen signals even for carbon nitride-functionalized systems, in line with the surface presence of very small gCN amounts [as confirmed by transmission electron microscopy (TEM) analyses]. The absence of tin signals proved the complete coverage of the FTO substrate.

For both bare iron oxide and the composite materials, the O/Fe atomic percentage (at. %) ratio values (2.2-2.3) were higher than the one expected for stoichiometric Fe_2O_3 (O/Fe = 1.5), due to the chemisorption of -OH groups on surface defects.[2, 6, 7] The obtained O/Fe values slightly higher after CoPi introduction, as expected.
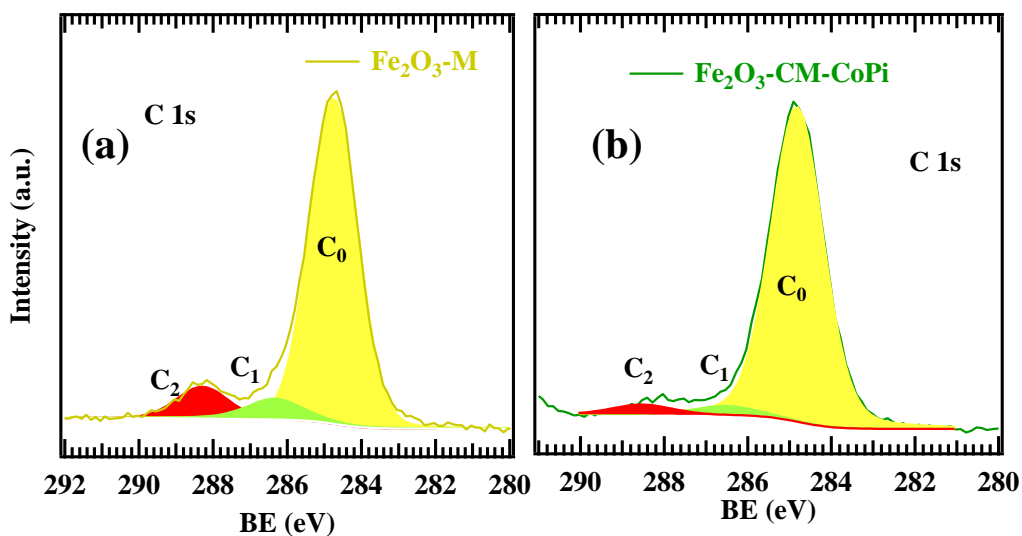
Fig. S9. Surface C1s photoelectron peaks for specimens Fe_2O_3-M (a) and Fe_2O_3-CM-CoPi (b). Color codes as in Fig. 2.

sample	C_0		C_1		C_2	
	BE (C_0) (eV)	% (C_0)	BE (C_1) (eV)	% (C_1)	BE (C_2) (eV)	% (C_2)
Fe_2O_3-M	284.8	83.8	286.4	7.4	288.4	8.8
Fe_2O_3-CM	284.8	84.0	286.5	7.9	288.5	8.1
Fe_2O_3-CM-CoPi	284.8	93.2	286.5	3.4	288.5	3.4

Table S1. BE (eV) and % of the various C1s components with respect to the overall C1s peak for the indicated specimens. Color codes as in Fig. 2.
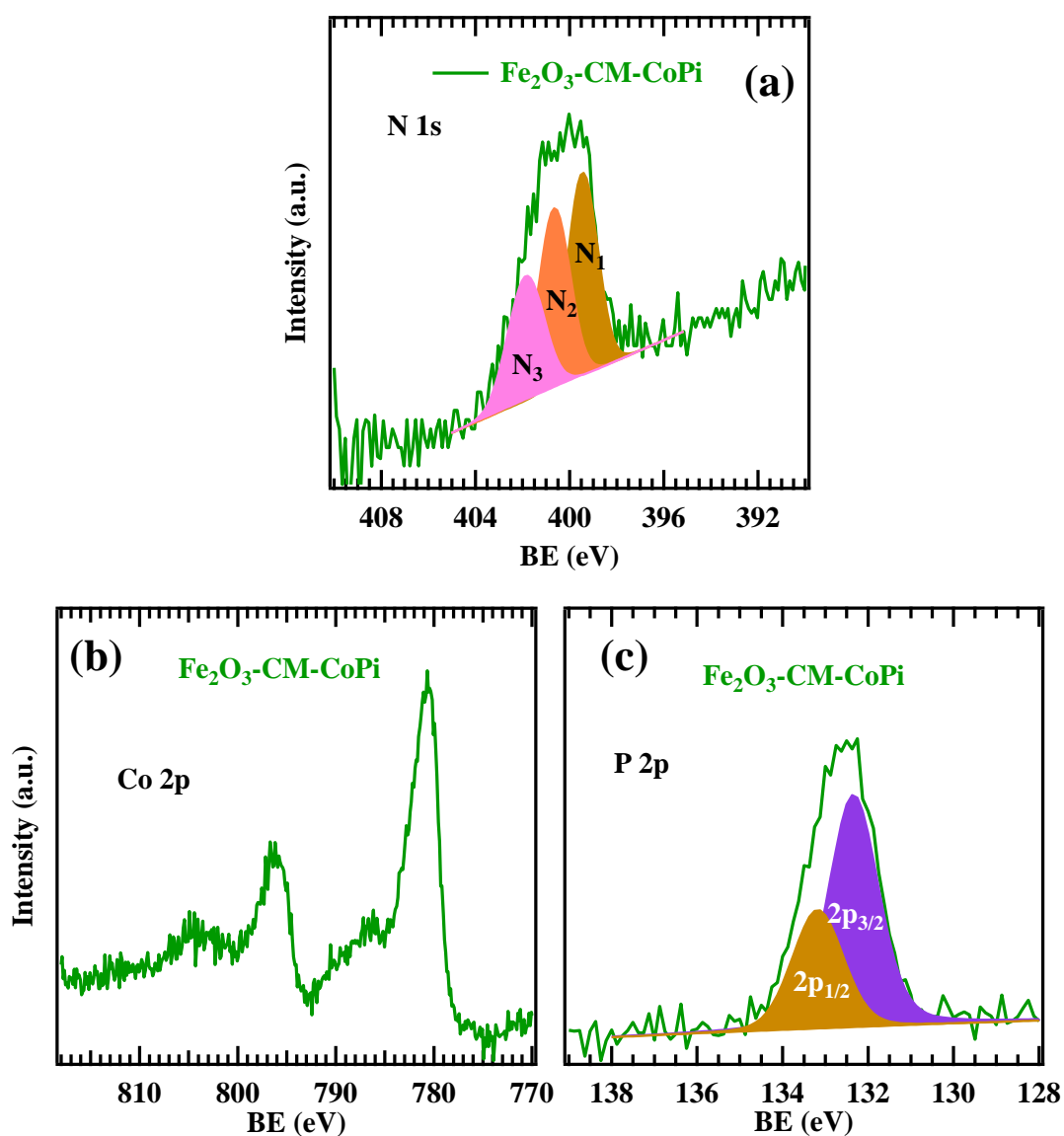
Fig. S10. (a) N1s, (b) Co2p, and (c) P2p photoelectron peaks for sample Fe_2O_3-CM-CoPi. Co at.% was estimated to be ≈ 3.0. Color codes for (a) as in Fig. 2.

sample	N₁		N₂		N₃	
	BE (N₁) (eV)	% (N₁)	BE (N₂) (eV)	% (N₂)	BE (N₃) (eV)	% (N₃)
Fe_2O_3-M	398.8	46.0	400.1	44.0	401.3	10.0
Fe_2O_3-CM	398.9	38.8	400.2	36.4	401.4	24.8
Fe_2O_3-CM-CoPi	398.9	38.6	400.2	35.4	401.4	26.0

Table S2. BE (eV) and % of the various N1s components with respect to the overall N1s peak for the indicated specimens. Color codes as in Fig. 2. The component associated to π-electron excitations in the heptazine rings of carbon nitride, expected at BE ≈ 404.2 eV and much weaker than the other ones,[3, 19-21] could not be detected due to the low overall nitrogen content.

sample	BE (Fe2p$_{3/2}$) (eV)	BE (Fe2p$_{1/2}$) (eV)	SOS (eV)
Fe$_2$O$_3$	711.2	724.7	13.5
Fe$_2$O$_3$-M	711.0	724.5	13.5
Fe$_2$O$_3$-CM	710.9	724.4	13.5
Fe$_2$O$_3$-CM-CoPi	710.9	724.4	13.5

Table S3. BE (eV) of Fe2p spin-orbit components for the target specimens. SOS = spin-orbit splitting.

For specimen Fe$_2$O$_3$-CM-CoPi (Fig. S10), both the Co2p and the P2p signals were clearly discernible. As regards the Co2p photopeak, the signal energy location [BE(Co2p$_{3/2}$) = 780.8; SOS = 15.4 eV] was in line with literature results for similar functionalized systems.[10, 22] In particular, basing on the shape of shake-up satellites at BE ≈ 7.6 eV higher than the corresponding spin-orbit split components, as well as the BE separation among the 2p$_{3/2}$ and 2p$_{1/2}$ components of ≈ 15.4 eV, cobalt centers were deemed to be primarily present as Co(II), with a likely minor contribution from Co(III) species.[23]

The P2p photopeak revealed the occurrence of phosphate groups in a single chemical environment [BE(P2p$_{3/2}$) = 132.4; SOS = 0.84 eV],[23-26] excluding the formation of phosphide moieties.[27, 28] Overall, these results proved the successful deposition of CoPi on the target samples.
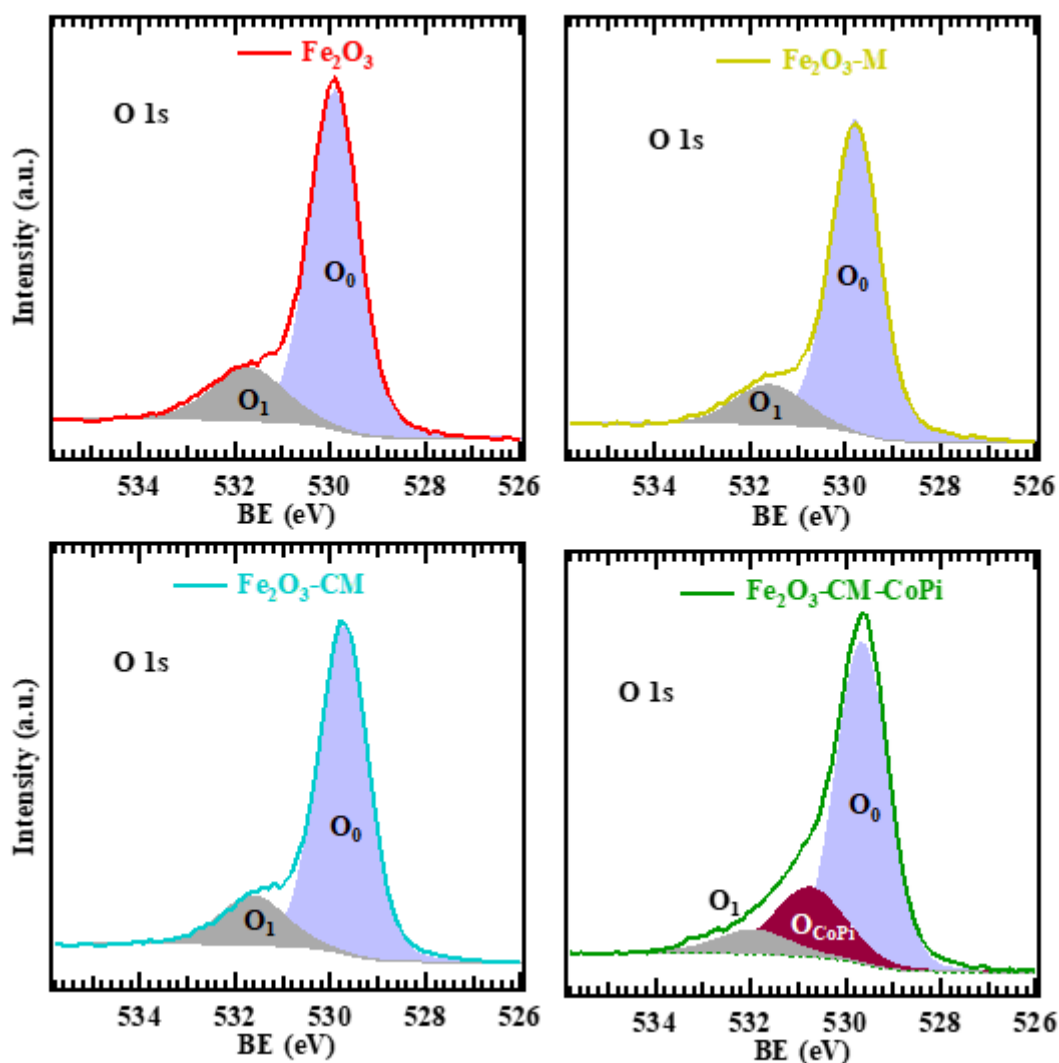
Fig. S11. Surface O1s photoelectron peaks for the indicated samples. Color codes as in Table S4.

For all CoPi-free samples, two different components contributed to the O1s signal (Fig. S11): the main one, **O_0**, related to lattice oxygen in Fe_2O_3,[29-35] and a second band, **O_1**, assigned to -OH groups adsorbed on surface vacancies.[8, 9, 25, 36-41] After functionalization with CoPi, a third component, ascribed to the presence of cobalt phosphate, could be identified (**O_{CoPi}**; see Table S4).[23, 25]

Upon going from bare Fe_2O_3 to Fe_2O_3-M and Fe_2O_3-CM, the **O_0** component underwent a progressive red shift (see also Table S4), whose entity was the same as the one experienced by Fe2p signals (compare Table S3). This variation confirmed the formation of a type-II Fe_2O_3/gCN heterojunction, as discussed in the main paper text, with a more efficient charge transfer occurring for Fe_2O_3-CM in comparison to Fe_2O_3-M.

sample	O_0		O_{CoPi}		O_1	
	BE (O_0) (eV)	% (O_0)	BE (O_{CoPi}) (eV)	% (O_{CoPi})	BE (O_1) (eV)	% (O_1)
Fe_2O_3	529.9	80.3	-	-	531.6	19.7
Fe_2O_3-M	529.7	85.8	-	-	531.6	14.2
Fe_2O_3-CM	529.6	81.9	-	-	531.6	18.1
Fe_2O_3-CM-CoPi	529.6	69.6	530.8	22.0	531.7	8.4

Table S4. BE (eV) and % of the various O1s components with respect to the overall O1s peak for the target specimens.
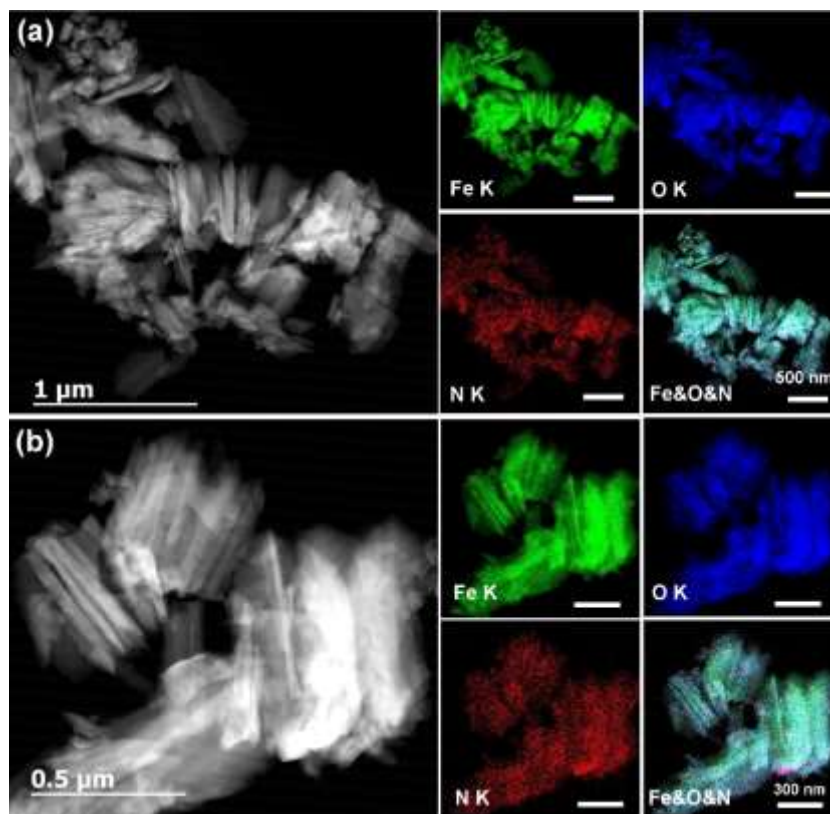
Fig. S12. HAADF-STEM overview and corresponding EDXS-STEM elemental maps of Fe K, O K, N K and overlaid color image for specimens Fe_2O_3-CM (a) and Fe_2O_3-M (b). Nitrogen signals, although very weak, well reproduced the surface morphology of the underlying iron oxide, suggesting the presence of a uniform and very thin gCN layer.
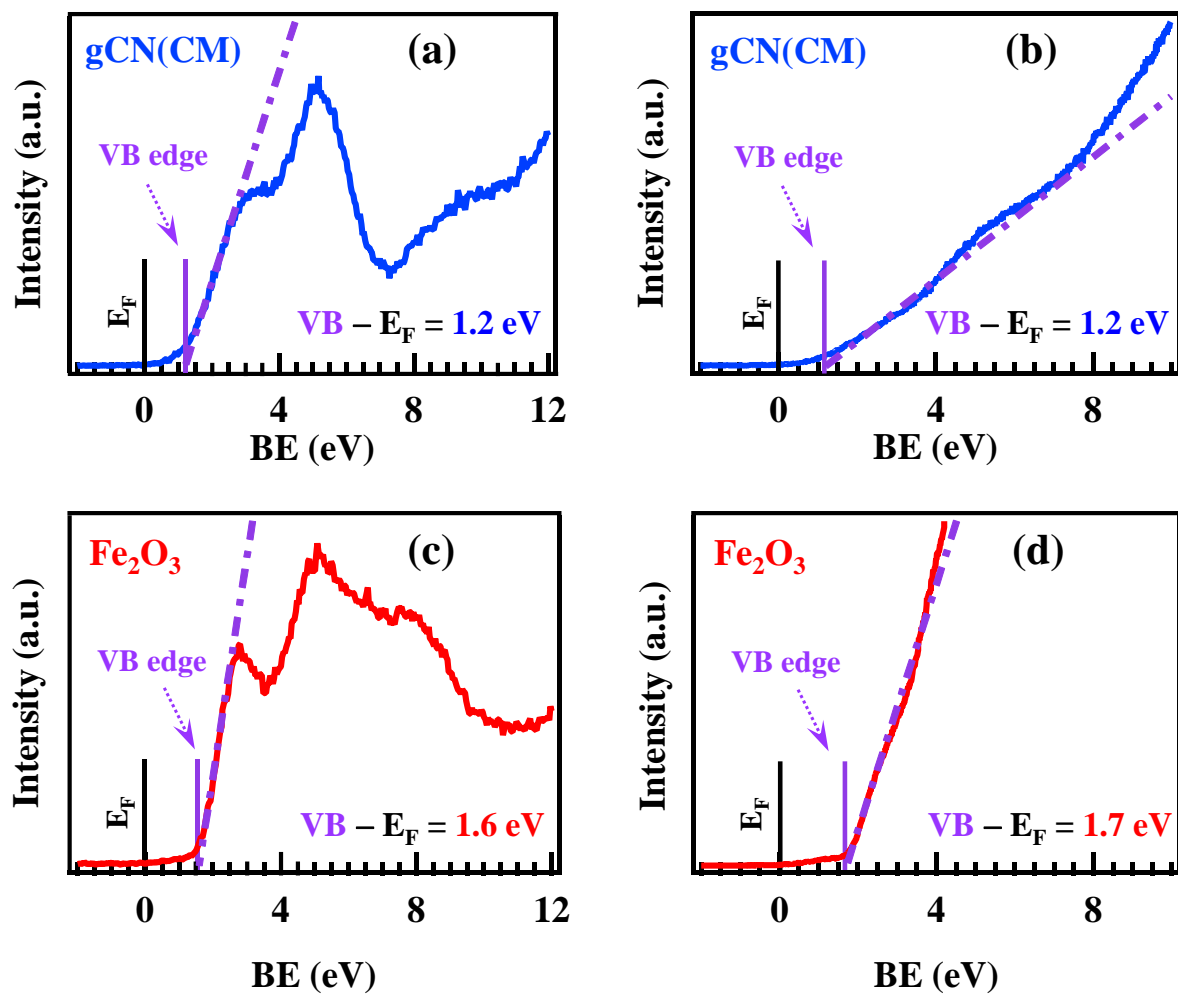
Fig. S13. XPS (a,c) and UPS (b,d) valence band spectra for gCN(CM) and Fe_2O_3 (E_F = Fermi level energy; VB = valence band).
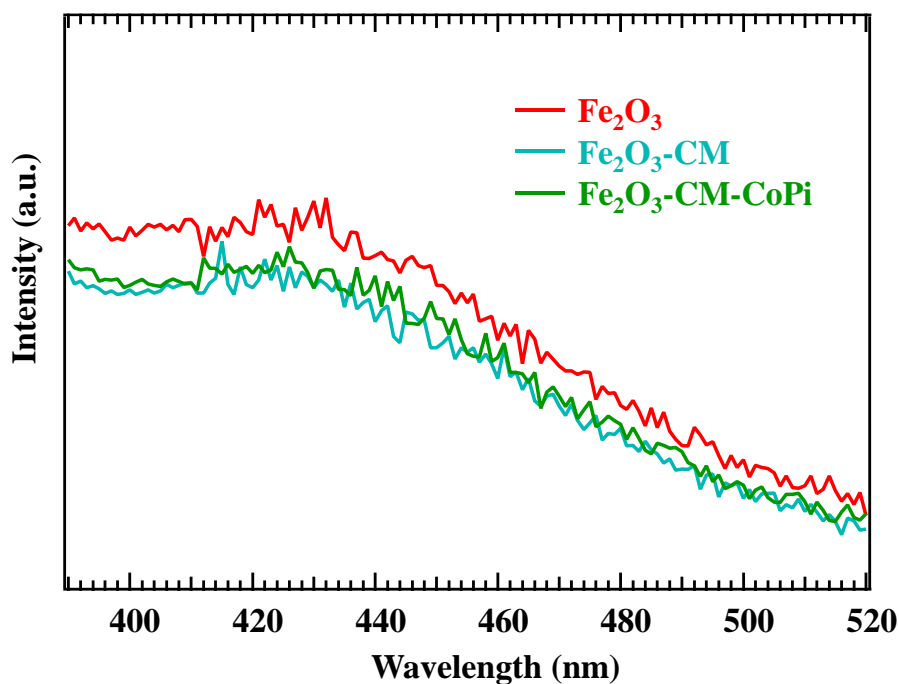
Fig. S14. Photoluminescence spectra obtained from Fe_2O_3, Fe_2O_3-CM and Fe_2O_3-CM-CoPi specimens.

The three PL spectra obtained for Fe_2O_3, Fe_2O_3-CM and Fe_2O_3-CM-CoPi samples (Fig. S14) show a very weak luminescence with negligible differences. As reported in the literature, Fe_2O_3 in bulk form, and with sufficiently developed crystalline particles, does not present any PL due to the local d-band transition nature and efficient energy relaxation.[42, 43] We also attribute the lack of photoluminescence at 450 nm, typical of gCN, to the very low carbon nitride amount present in the target nanocomposites, and to the PL quenching due to the Fe_2O_3/gCN junction formation.

§ S-2.3. Photolectrochemical tests and related analyses

Sample	Electrolyte	$j_{1.5}$ (mA/cm^2)	Onset potential @ 0.02 mA/cm^2 (V vs. RHE)	Tafel slope (mV/dec)	ABPE$_{max}$ × 10^{-3} (%)	E$_{Wmax}$ (V$_{RHE}$)
Fe$_2$O$_3$	Simulated alkaline seawater (0.5 M KOH + 0.5 M NaCl)	0.50	1.16	141	3.68	1.08
Fe$_2$O$_3$-M		0.61	1.15	133	4.65	1.07
Fe$_2$O$_3$-CM		0.65	1.11	124	7.61	1.03
Fe$_2$O$_3$-CoPi		0.68	1.07	111	12.84	1.03
Fe$_2$O$_3$-M-CoPi		0.76	1.06	108	13.44	1.02
Fe$_2$O$_3$-CM-CoPi		0.85	1.03	102	26.40	0.98

Table S5. Oxygen evolution reaction (OER) performances for photoelectrocatalysts based on Fe$_2$O$_3$ and gCN, both as such and functionalized with CoPi, in simulated alkaline seawater splitting. J$_{1.5}$ corresponds to the current density measured at 1.5 V vs. RHE. The potential of maximum efficiency (E$_{Wmax}$) corresponds to the maximum in each of the applied bias photon-to-current efficiency (ABPE) curves in Fig. 5b.

Sample	Electrolyte	$j_{1.5}$ (mA/cm^2)	Onset potential @ 0.02 mA/cm^2 (V $vs.$ RHE)	Tafel slope (mV/dec)	ABPE$_{max}$ × 10^{-3} (%)	E$_{Wmax}$ (V$_{RHE}$)
Fe$_2$O$_3$-CoPi	Real alkaline seawater (pH: 13.58)	0.66	1.15	144	5.13	1.07
Fe$_2$O$_3$-M-CoPi		0.71	1.10	136	6.40	1.06
Fe$_2$O$_3$-CM-CoPi		0.79	1.09	125	7.94	1.05

Table S6. OER performances for photoelectrocatalysts based on Fe$_2$O$_3$ and gCN functionalized with CoPi, in Adriatic seawater splitting. E$_{Wmax}$ values correspond to the maxima in ABPE curves displayed in Fig. 7b.

Material	Electrolyte	$j_{1.5}$ (mA/cm²)	Tafel slope (mV/dec)	Ref.
Mo-doped g-C$_3$N$_4$ [a]	Simulated alkaline seawater (1.0 M KOH + 0.5 M NaCl)	≈1	354.9	[12]
NiFe (LDH)/Mo-doped g-C$_3$N$_4$ [a]		≈1-5	≈133-169	[12]
Fe$_2$O$_3$ [b]	Simulated alkaline seawater (1.0 M NaOH + 35 g/L sea salt)	≈0.35	n.a.	[14]
Fe$_2$O$_3$-TiO$_2$ [b]		≈1.0	n.a.	[14]

Table S7. OER performances for previously reported electrocatalysts based on Fe$_2$O$_3$ or gCN in simulated seawater splitting. [a] dark conditions. [b] light conditions. LDH = layered double hydroxides. *n.a.* = not available.

Material	Electrolyte	$j_{1.5}$ (mA/cm^2)	Tafel slope (mV/dec)	Ref.
TiO$_2$@g-C$_3$N$_4$ [a]	Natural seawater (pH = 6.4)	≈1.3	n.a.	44
TiO$_2$@g-C$_3$N$_4$@CoPi [a]		≈1.7	n.a.	44
WO$_3$@g-C$_3$N$_4$ [a]		≈0.95	n.a.	45
Ru, Ni-doped Fe$_2$O$_3$ [b]	Real alkaline seawater (1.0 M KOH)	≈0	≈60-80	35

Table S8. OER performances for previously reported electrocatalysts based on Fe$_2$O$_3$ or gCN in seawater splitting. [a] light conditions. [b] dark conditions. *n.a.* = not available.
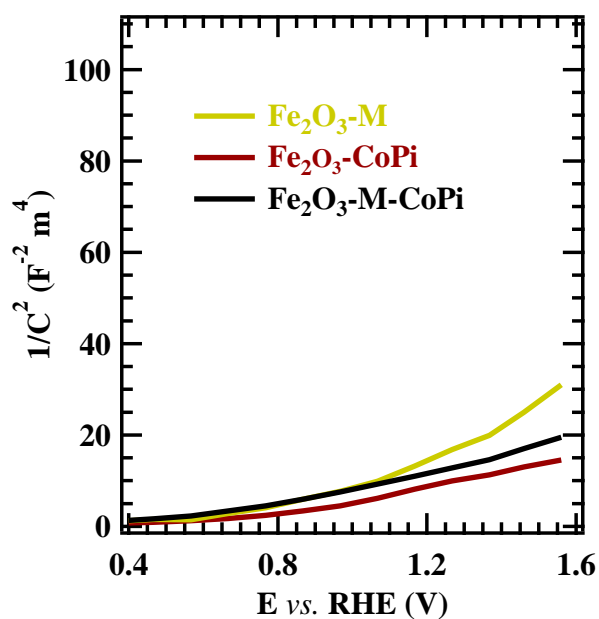
Fig. S15. Mott-Schottky plots as a function of the applied potential for specimens Fe_2O_3-M, Fe_2O_3-CoPi, and Fe_2O_3-M-CoPi.

Sample	V_{FB} vs. RHE (V)	N_D (m^{-3})
Fe_2O_3	0.86	2.1×10^{26}
Fe_2O_3-M	0.82	5.4×10^{26}
Fe_2O_3-CM	0.80	7.2×10^{26}
Fe_2O_3-CoPi	0.80	9.8×10^{26}
Fe_2O_3-M-CoPi	0.78	1.0×10^{27}
Fe_2O_3-CM-CoPi	0.74	1.1×10^{27}

Table S9. Flat band potentials (V_{FB}) and majority charge carrier concentration (N_D) obtained from Mott-Schottky plots at 1 kHz.
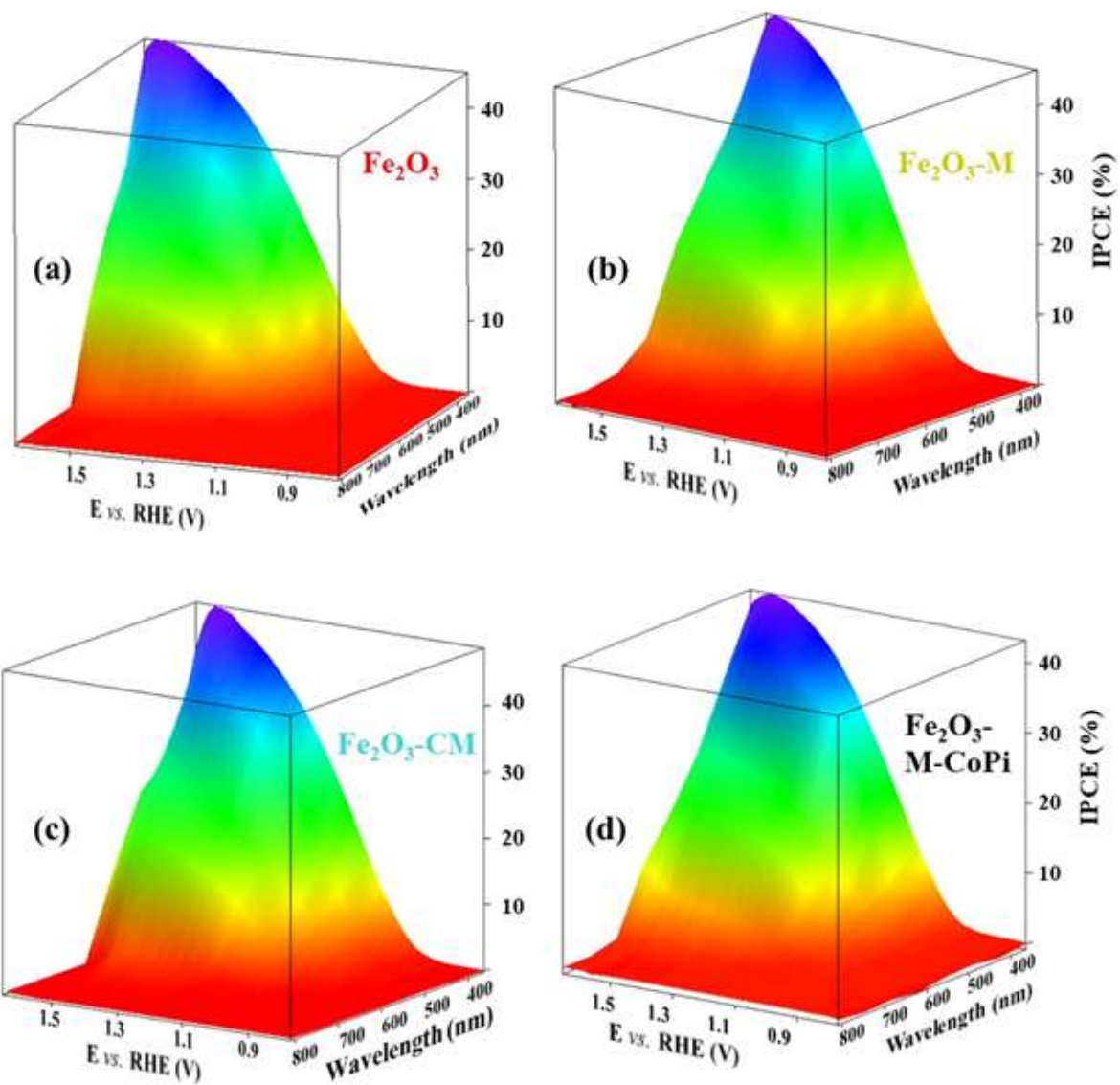
Fig. S16. Incident photon-to-current conversion efficiency (IPCE, %) spectra for Fe$_2$O$_3$ (a), Fe$_2$O$_3$-M (b), Fe$_2$O$_3$-CM (c), and Fe$_2$O$_3$-M-CoPi (d).

Intensity modulated photocurrent spectroscopy (IMPS) is a form of impedance spectroscopy measuring the photocurrent phase shift in relation to a sinusoidal modulation of the light source.[46, 47] The IMPS response as a function of frequency can be expressed as:

$$j_{photo} = j_{hole} \frac{C_H}{C_H + C_{SC}} \frac{(k_{inj} + i\omega)}{(k_{inj} + k_{rec} + i\omega)} \left[\frac{1}{1 + i\omega\tau_c} \right] \tag{S6}$$

where τ_C is the cell time constant, k_{rec} and k_{inj} are *pseudo*-first order rate constants for electron-hole recombination and charge injection (in the electrolyte), respectively, and j_{hole} is the photocurrent density before recombination. C_H and C_{SC} are the capacitances of the Helmholtz layer and the space charge region, respectively. A normalized and simulated Nyquist plot $\frac{j_{photo}}{j_{hole}}$ is reported in Fig. S17. Assuming that τ_C is at least two decades smaller than $1/(k_{rec} + k_{inj})$, two important numbers can be identified in the plot, *i.e.* the low frequency intercept (LFI):

$$\text{LFI} = j_{hole} \frac{C_H}{C_H + C_{SC}} \frac{(k_{inj})}{(k_{inj} + k_{rec})} \tag{S7}$$

and the high frequency intercept (HFI):

$$\text{HFI} = j_{hole} \frac{C_H}{C_H + C_{SC}}, \tag{S8}$$

as indicated in Fig. S17. Combining equations (S7) and (S8), the ratio HFI/LFI corresponds to $k_{inj}/(k_{inj} + k_{rec})$.

The other interesting point in Fig. S17 corresponds to the resonance frequency (the maximum in the positive quadrant): $\omega_{max} = k_{inj} + k_{rec}$. Since ω_{max} can be easily obtained from the Nyquist plot, it is straightforward to calculate k_{inj} and k_{rec}.

In Figs. S18 and S19, each spectrum is normalized to ensure that the HFI = $\frac{C_H}{C_H + C_{SC}}$.
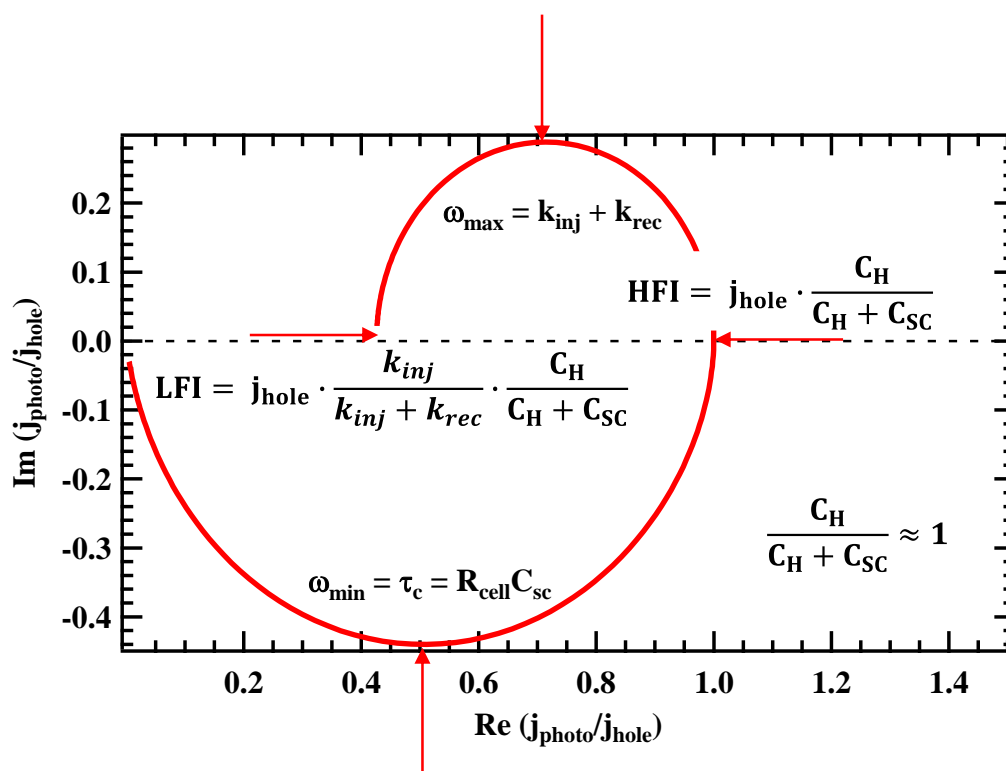
Fig. S17. Simulated IMPS Nyquist plot. The points in the figure enabling to calculate k_{inj} and k_{rec} are LFI, HFI and ω_{max}, indicated by arrows. The high frequency intercept should occur at unity, since the measured current is equal to the hole current (*i.e.* no recombination), assuming $C_H/(C_H+C_{sc}) \approx 1$. The normalized low frequency intercept corresponds to the fraction of the hole flux that undergoes interfacial electron transfer, $k_{inj}/k_{inj}+k_{rec}$.
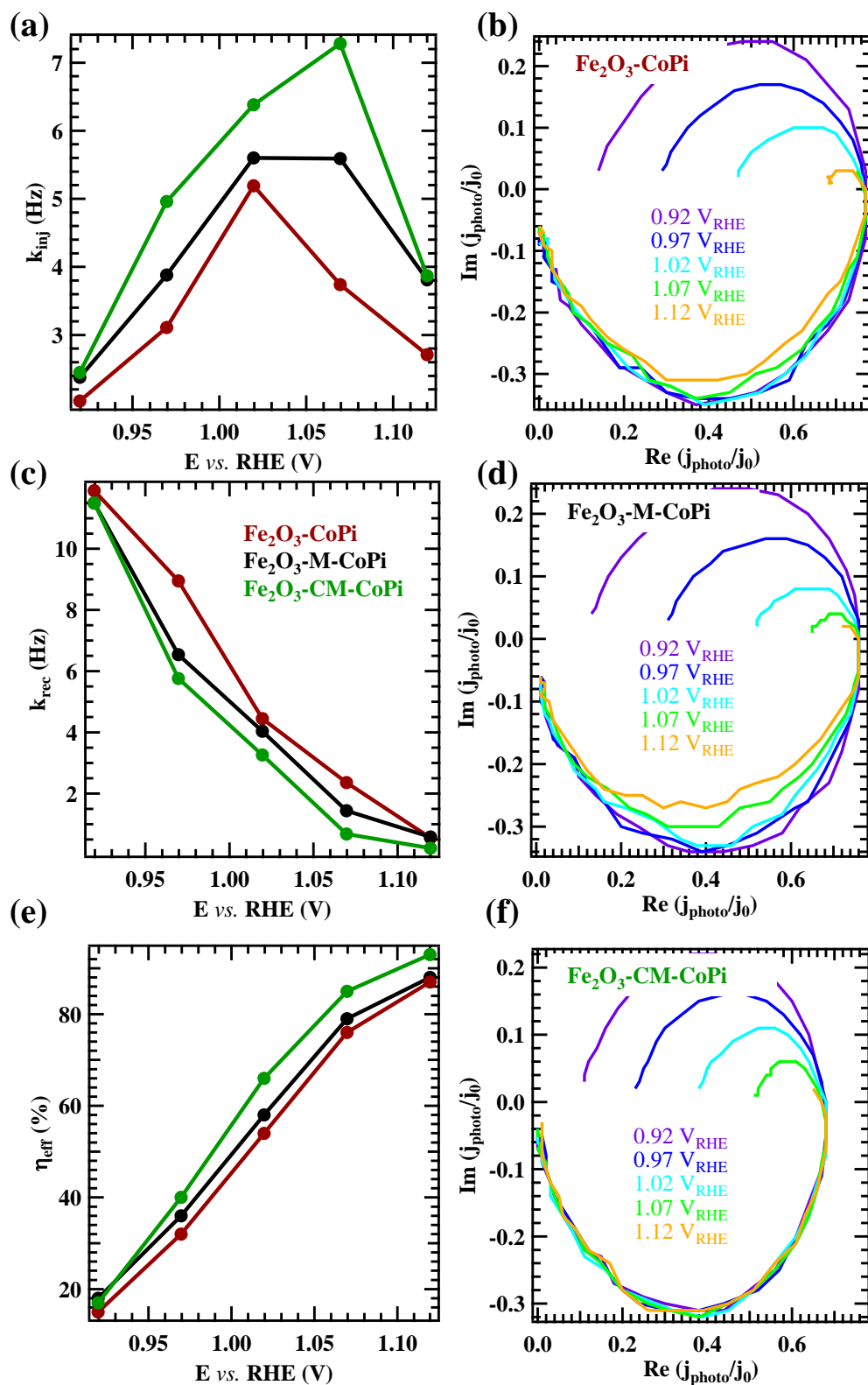
Fig. S18. (a) k_{inj}, (c) k_{rec}, and (e) charge transfer efficiency values (η_{eff}; defined as in the main paper text, Fig. 8 caption) for samples Fe₂O₃-CoPi, Fe₂O₃-M-CoPi and Fe₂O₃-CM-CoPi. IMPS measurements were carried out in 0.1 M KOH aqueous solutions, before electrochemical tests in seawater. The corresponding normalized Nyquist IMPS plots are displayed in (b), (d) and (f).
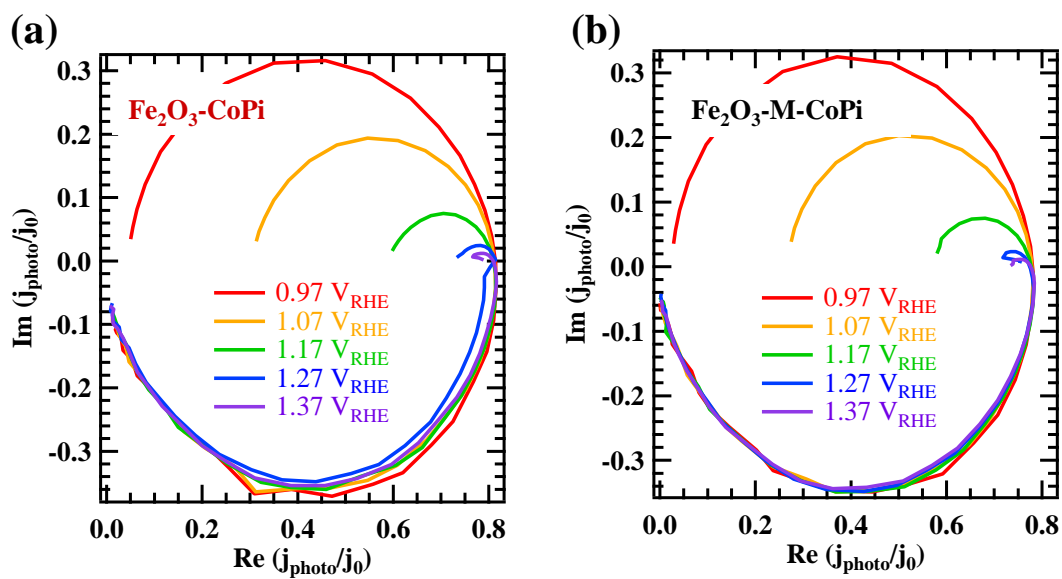
Fig. S19. Normalized Nyquist IMPS plots for samples Fe$_2$O$_3$-CoPi (a), and Fe$_2$O$_3$-M-CoPi (b). IMPS measurements were carried out in 0.1 M KOH aqueous solutions, after testing the specimens in seawater.

§ S-2.4 Characterization after photoelectrochemical tests
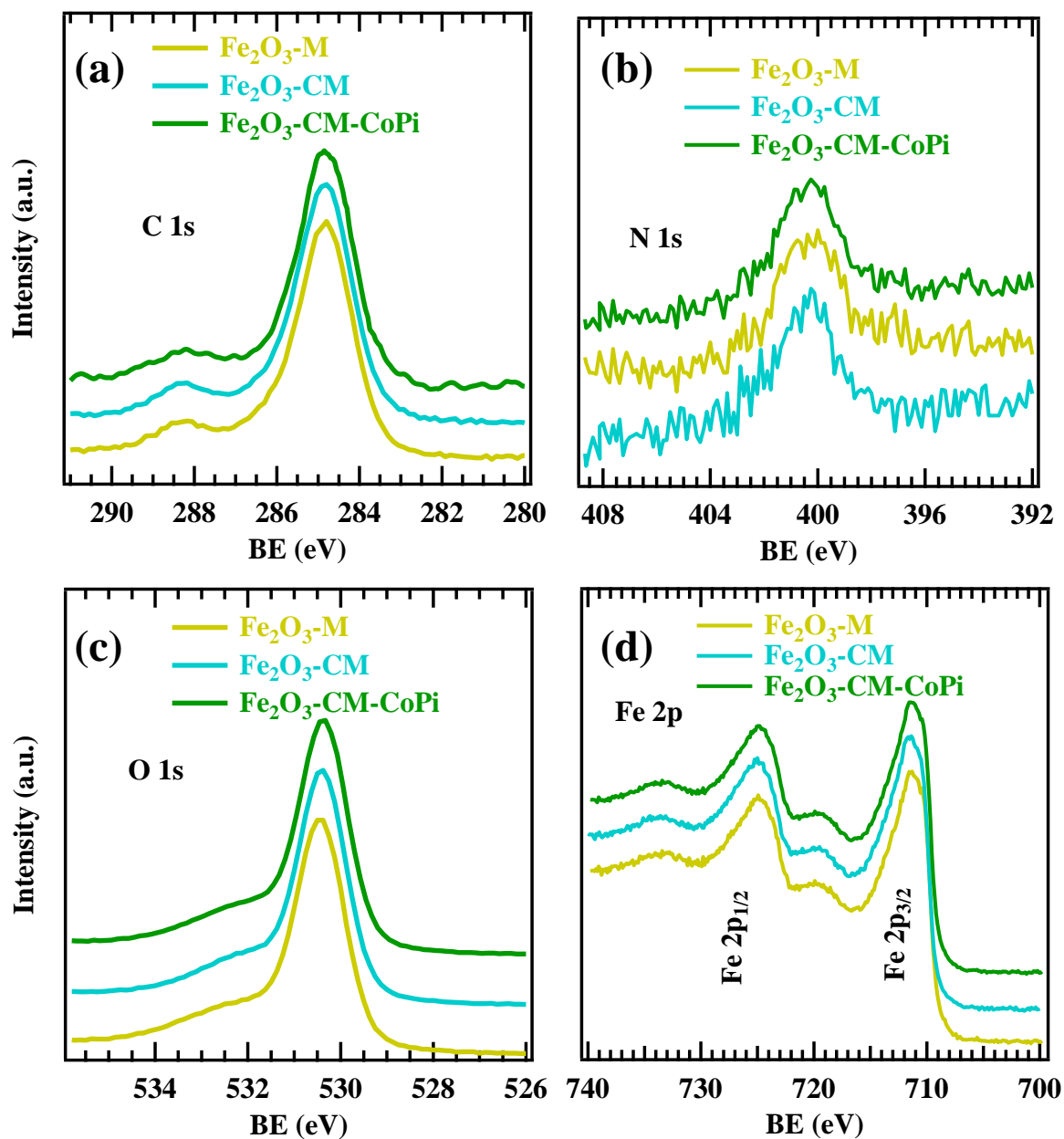
Fig. S20. XPS analysis for the indicated specimens after storage under ambient conditions for six months, during which each sample was photoelectrochemically tested in Adriatic seawater every 90 days: (a) C1s, (b) N1s, (c) O1s, and (d) Fe2p photoelectron peaks.
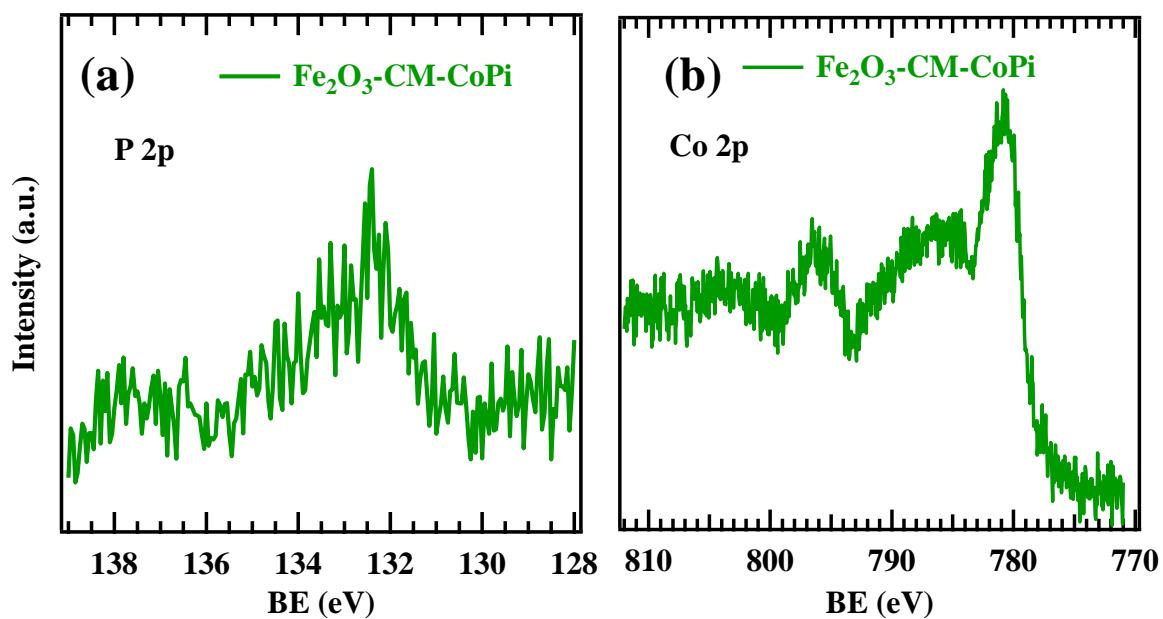
Fig. S21. XPS analysis for Fe₂O₃-CM-CoPi after storage under ambient conditions for six months, during which the sample was photoelectrochemically tested in Adriatic seawater every 90 days: (a) P2p, and (b) Co2p photoelectron peaks. Compared to the Co2p signals detected on the same sample prior electrochemical tests (see Fig. S10b), the BE separation between the main spin orbit components slightly decreased to 15.2 eV, suggesting a likely increase of the Co(III)/Co(II) ratio, in line with literature results on similar CoPi-containing systems.[23]

Fe$_2$O$_3$-CM-CoPi

(a)

Fe$_2$O$_3$-CM

(b)
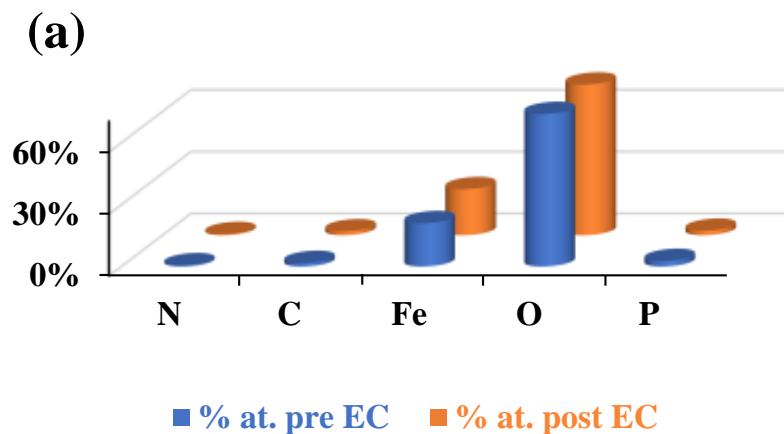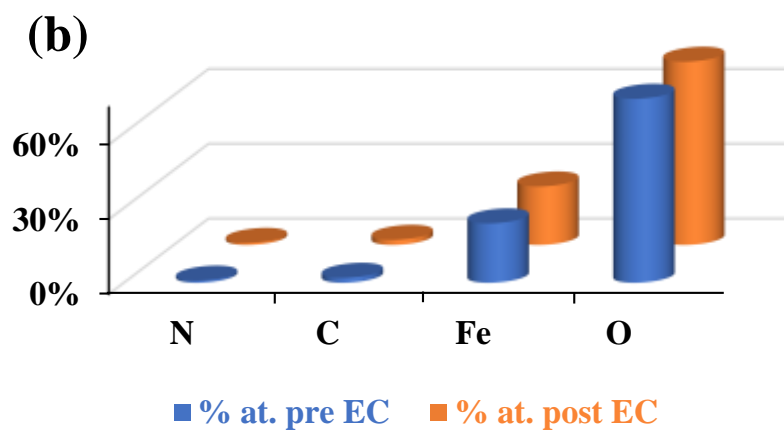
Fig. S22. Atomic percentage (%) values for the indicated specimens before photoelectrochemical tests (in blue), and after storage under ambient conditions for six months (in orange), during which each sample was photoelectrochemically tested in Adriatic seawater every 90 days.
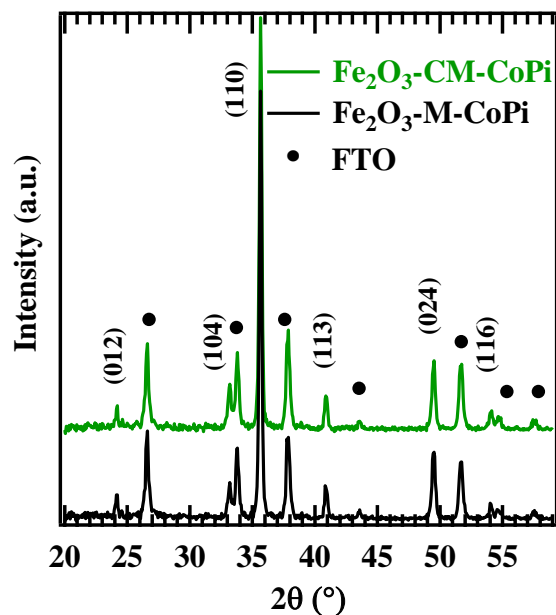
Fig. S23. XRD patterns of Fe$_2$O$_3$-M-CoPi and Fe$_2$O$_3$-CM-CoPi specimens after storage under ambient conditions for six months, during which each sample was photoelectrochemically tested in Adriatic seawater every 90 days. The pattern of the FTO-coated glass substrate is also reported for comparison. All the indexed peaks correspond to α-Fe$_2$O$_3$ (*hematite*) reflections.[18] CoPi presence could never be revealed, due to its low amount (compare Fig. S10 caption) and/or amorphous nature.[48, 49]
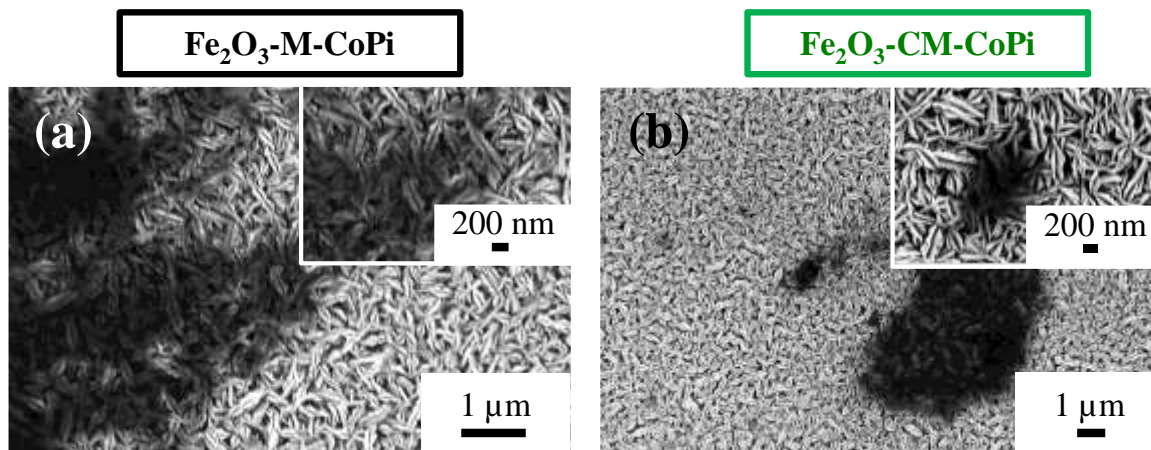
Fig. S24. Representative FE-SEM micrographs for specimens Fe$_2$O$_3$-M-CoPi (a) and Fe$_2$O$_3$-CM-CoPi (b) after storage under ambient conditions for six months, during which each sample was photoelectrochemically tested in Adriatic seawater every 90 days.

References

1. D. Barreca, L. Bigiani, M. Klotzsche, A. Gasparotto, R. Seraglia, C. Jandl, A. Pöthig, E. Fois, L. Vanin, G. Tabacchi, M. Roverso, S. Bogialli, E. Callone, S. Dirè and C. Maccato, *Mater. Chem. Phys.*, 2022, **277**, 125534.

2. D. Barreca, G. Carraro, A. Gasparotto, C. Maccato, C. Sada, A. P. Singh, S. Mathur, A. Mettenbörger, E. Bontempi and L. E. Depero, *Int. J. Hydrogen Energy*, 2013, **38**, 14189-14199.

3. M. Benedet, G. A. Rizzi, A. Gasparotto, O. I. Lebedev, L. Girardi, C. Maccato and D. Barreca, *Chem. Eng. J.*, 2022, **448**, 137645.

4. Y.-S. Jun, E. Z. Lee, X. Wang, W. H. Hong, G. D. Stucky and A. Thomas, *Adv. Funct. Mater.*, 2013, **23**, 3661-3667.

5. M. W. Kanan and D. G. Nocera, *Science*, 2008, **321**, 1072-1075.

6. L. Bigiani, D. Barreca, A. Gasparotto, T. Andreu, J. Verbeeck, C. Sada, E. Modin, O. I. Lebedev, J. R. Morante and C. Maccato, *Appl. Catal., B*, 2021, **284**, 119684.

7. G. Carraro, C. Maccato, A. Gasparotto, K. Kaunisto, C. Sada and D. Barreca, *Plasma Processes Polym.*, 2016, **13**, 191-200.

8. R. Khurram, Z. U. Nisa, A. Javed, Z. Wang and M. A. Hussien, *Molecules*, 2022, **27**, 1442.

9. F. Wang, R. Ou, H. Yu, Y. Lu, J. Qu, S. Zhu, L. Zhang and M. Huo, *Appl. Surf. Sci.*, 2021, **565**, 150597.

10. M. E. A. Warwick, K. Kaunisto, D. Barreca, G. Carraro, A. Gasparotto, C. Maccato, E. Bontempi, C. Sada, T.-P. Ruoko, S. Turner and G. Van Tendeloo, *ACS Appl. Mater. Interfaces*, 2015, **7**, 8667-8676.

11. M. C. Biesinger, B. P. Payne, A. P. Grosvenor, L. W. M. Lau, A. R. Gerson and R. S. C. Smart, *Appl. Surf. Sci.*, 2011, **257**, 2717-2730.

12. Y. Du, Y. Zhang, X. Pu, X. Fu, X. Li, L. Bai, Y. Chen and J. Qian, *Chemosphere*, 2023, **312**, 137203.

13. T. u. Haq and Y. Haik, *ACS Sustainable Chem. Eng.*, 2022, **10**, 6622-6632.

14. D. Barreca, G. Carraro, A. Gasparotto, C. Maccato, M. E. A. Warwick, K. Kaunisto, C. Sada, S. Turner, Y. Gönüllü, T.-P. Ruoko, L. Borgese, E. Bontempi, G. Van Tendeloo, H.

Lemmetyinen and S. Mathur, *Adv. Mater. Interfaces*, 2015, **2**, 1500313.

15. B. Klahr, S. Gimenez, F. Fabregat-Santiago, T. Hamann and J. Bisquert, *J. Am. Chem. Soc.*, 2012, **134**, 4294-4302.

16. A. Hankin, F. E. Bedoya-Lora, J. C. Alexander, A. Regoutz and G. H. Kelsall, *J. Mater. Chem. A*, 2019, **7**, 26162-26176.

17. J. Mendham, R. C. Denney, J. D. Barnes, M. J. K. Thomas, *Vogel's Quantitative Chemical Analysis* (6th ed.), Prentice Hall, New York, 2000.

18. Pattern N° 33-0664, JCPDS (2000).

19. M. Benedet, G. A. Rizzi, A. Gasparotto, N. Gauquelin, A. Orekhov, J. Verbeeck, C. Maccato and D. Barreca, *Appl. Surf. Sci.*, 2023, **618**, 156652.

20. M. Benedet, A. Gasparotto, G. A. Rizzi, D. Barreca and C. Maccato, *Surf. Sci. Spectra*, 2022, **29**, 024001.

21. M. Benedet, G. A. Rizzi, D. Barreca, A. Gasparotto and C. Maccato, *Surf. Sci. Spectra*, 2023, **30**, 014004.

22. K. J. McDonald and K.-S. Choi, *Chem. Mater.*, 2011, **23**, 1686-1693.

23. R. Zhang, G. van Straaten, V. di Palma, G. Zafeiropoulos, M. C. M. van de Sanden, W. M. M. Kessels, M. N. Tsampas and M. Creatore, *ACS Catal.*, 2021, **11**, 2774-2785.

24. X. An, C. Hu, H. Lan, H. Liu and J. Qu, *ACS Appl. Mater. Interfaces*, 2018, **10**, 6424-6432.

25. L. Fu, H. Yu, C. Zhang, Z. Shao and B. Yi, *Electrochim. Acta*, 2014, **136**, 363-369.

26. T. H. Jeon, G.-h. Moon, H. Park and W. Choi, *Nano Energy*, 2017, **39**, 211-218.

27. W. Mei, X. Yang, L. Li, Y. Tong, Y. Lei, P. Li and Z. Zheng, *ACS Sustainable Chemistry & Engineering*, 2020, **8**, 3606-3616.

28. G. Liu, Y. Zhao, R. Yao, N. Li, M. Wang, H. Ren, J. Li and C. Zhao, *Chemical Engineering Journal*, 2019, **355**, 49-57.

29. Y. Geng, D. Chen, N. Li, Q. Xu, H. Li, J. He and J. Lu, *Appl. Catal., B*, 2021, **280**, 119409.

30. Y. Wu, J. Ward-Bond, D. Li, S. Zhang, J. Shi and Z. Jiang, *ACS Catal.*, 2018, **8**, 5664-5674.

31. L. Zhang, X. Zhang, C. Wei, F. Wang, H. Wang and Z. Bian, *Chem. Eng. J.*, 2022, **435**, 134873.

32. J. K. George, A. Bhagat, B. Bhaduri and N. Verma, *Catal. Lett.*, 2023, **153**, 419-431.

33. Z. Pan, G. Zhang and X. Wang, *Angew. Chem. Int. Ed.*, 2019, **58**, 7102-7106.

34. Q. Xu, B. Zhu, C. Jiang, B. Cheng and J. Yu, *Sol. RRL*, 2018, **2**, 1800006.

35. T. Cui, X. Zhai, L. Guo, J.-Q. Chi, Y. Zhang, J. Zhu, X. Sun and L. Wang, *Chin. J. Catal.*, 2022, **43**, 2202-2211.

36. N. A. Arzaee, M. F. M. Noh, N. S. H. M. Ita, N. A. Mohamed, S. N. F. M. Nasir, I. N. N. Mumthas, A. F. Ismail and M. A. M. Teridi, *Dalton Trans.*, 2020, **49**, 11317-11328.

37. Z. Jiang, W. Wan, H. Li, S. Yuan, H. Zhao and P. K. Wong, *Adv. Mater.*, 2018, **30**, 1706108.

38. Y. Shen, Q. Han, J. Hu, W. Gao, L. Wang, L. Yang, C. Gao, Q. Shen, C. Wu, X. Wang, X. Zhou, Y. Zhou and Z. Zou, *ACS Appl. Energy Mater.*, 2020, **3**, 6561-6572.

39. J. Wang, X. Zuo, W. Cai, J. Sun, X. Ge and H. Zhao, *Dalton Trans.*, 2018, **47**, 15382-15390.

40. N. A. Arzaee, M. F. Mohamad Noh, N. S. H. Mohd Ita, N. A. Mohamed, S. N. F. Mohd Nasir, I. N. Nawas Mumthas, A. F. Ismail and M. A. Mat Teridi, *Dalton Trans.*, 2020, **49**, 11317-11328.

41. Y. Yang, L. Liu, Q. Qi, F. Chen, M. Qiu, F. Gao and J. Chen, *Catal. Commun.*, 2020, **143**, 106047.

42. Y. Zhang, W. Liu, C. Wu, T. Gong, J. Wei, M. Ma, K. Wang, M. Zhong and D. Wu, *Mater. Res. Bull.*, 2008, **43**, 3490-3494.

43. Y. P. He, Y. M. Miao, C. R. Li, S. Q. Wang, L. Cao, S. S. Xie, G. Z. Yang, B. S. Zou and C. Burda, *Phys. Rev. B*, 2005, **71**, 125411.

44. Y. Li, R. Wang, H. Li, X. Wei, J. Feng, K. Liu, Y. Dang and A. Zhou, *J. Phys. Chem. C*, 2015, **119**, 20283-20292.

45. Y. Li, X. Wei, X. Yan, J. Cai, A. Zhou, M. Yang and K. Liu, *Phys. Chem. Chem. Phys.*, 2016, **18**, 10255-10261.

46. E. A. Ponomarev and L. M. Peter, *J. Electroanal. Chem.*, 1995, **396**, 219-226.

47. L. M. Peter and D. Vanmaekelbergh, in *Advances in Electrochemical Science and Engineering*, (eds R.C. Alkire and D.M. Kolb), Wiley, 1999, pp. 77-163.

48. A. Qin, W. Fang, Y. Lin, R. Xv and L. Fu, *New J. Chem.*, 2022, **46**, 359-369.

49. W. Fang, Y. Lin, R. Xv, X. Shang and L. Fu, *Electrochim. Acta*, 2023, **437**, 141511.